Capabilities of BIOMASS Tomography for Investigating Tropical Forests

Dinh Ho Tong Minh, Stefano Tebaldini, Fabio Rocca, Thuy Le Toan, Ludovic Villard, and Pascale C. Dubois-Fernandez

I. Introduction

THE synthetic aperture radar (SAR) mission BIOMASS was selected in 2013 as the next European Space Agency (ESA) Earth Explorer Core Mission. BIOMASS's primary objectives are focused on providing a global mapping of the forest height and the above-ground biomass (AGB), which are key elements to the global carbon cycle [1], [2]. To achieve this goal, the BIOMASS mission features a fully polarimetric SAR operating at P-band to ensure that the transmitted wave can penetrate the vegetation layer down to the ground even in a dense tropical forest. The satellite will be operated in two different observation phases, i.e., the tomographic phase performed just after the commissioning phase and the nominal phase implemented with a drifting orbit to allow the acquisitions of interferometric image pairs [1]. During the tomographic phase, the system will be able to gather multiple acquisitions characterized by small baselines and a repeat interval of about three–four days, thus allowing the SAR tomography (TomoSAR) imaging of the vegetation layer [3]–[7]. This will potentially lead to a better understanding of how long wavelength radar signals interact with forests and, thus, will provide useful inputs for improving inversion based on polarimetric SAR intensity and on polarimetric interferometric SAR inversion during the nominal phase.

For forests, airborne TomoSAR imaging allows us to retrieve the vertical structure of the vegetation, which would be one of the key elements for the assessment of the forest AGB. It was shown in [7] that, at the Paracou tropical forest site, the signal coming from upper vegetation layers exhibits a much more stable connection to the AGB. This finding was used to define a simple AGB estimator based on the backscatter associated with upper layers only (i.e., ground contributions were discarded), resulting in a final accuracy with respect to *in situ* data of about 10% at a resolution of 1.5 ha [7]. This result advocates in favor of TomoSAR methods to map the forest AGB. Such finding is encouraging as a high accuracy estimate of the AGB is required particularly for tropical forests.

However, there are three main factors expected to have significant impact on the performance of the BIOMASS tomography. First, the limited bandwidth allowed for the BIOMASS system by the International Telecommunication Union (ITU) regulations, i.e., 6 MHz, has been thought as a strong limitation to the use of the P-band SAR data [8]. Second is the interaction with the ionosphere of the P-band waves, resulting in disturbances such as Faraday rotation and residual phase screens [9], [10]. Finally, the third factor is the factor related to temporal decorrelation, i.e., instantaneous, short-term, and long-term decorrelation mechanisms [11]. The impact of the ionosphere was shown in [12] to be not critical to TomoSAR. The impact of the temporal decorrelation is currently under analysis in the frame of the TropiScat campaign [13], [14],

Manuscript received July 16, 2013; revised December 20, 2013, March 18, 2014, and May 27, 2014; accepted June 3, 2014. Date of publication July 8, 2014; date of current version August 12, 2014. This work was supported in part by the European Space Agency and in part by the Centre National d'Etudes Spatiales/Terre, Océan, Surfaces Continentales, Atmosphére (TOSCA).

D. Ho Tong Minh, T. Le Toan, and L. Villard are with the Centre d'Etudes Spatiales de la Biosphère (CESBIO), 31401 Toulouse, France (e-mail: htmdinhrs@gmail.com).

S. Tebaldini and F. Rocca are with the Dipartimento di Ingegneria Elettronica, Informazione e Bioingegneria, Politecnico di Milano, 20133 Milano, Italy (e-mail: tebaldini@elet.polimi.it; rocca@elet.polimi.it).

P. C. Dubois-Fernandez is with the Department of Electromagnetism and Radar, Office National d'Etudes et de Recherches Aérospatiales (ONERA), 31000 Toulouse, France (e-mail: pascale.dubois-fernandez@onera.fr).

Color versions of one or more of the figures in this paper are available online.

where continuous ground-based acquisitions are gathered over a time span of a year.

In this paper, we focus on the first of the three factors aforementioned, i.e., on the impact of the bandwidth on the BIOMASS tomography. Bandwidth reduction (as compared with typical airborne cases) causes the SAR resolution cell to spread along the line-of-sight (LOS). At the proposed incidence angle of about 25° of BIOMASS, this translates into a significant resolution loss not only in the horizontal direction but also in the vertical direction. As a result, the BIOMASS tomography is hindered by two different factors compared with airborne tomography, i.e., a significant reduction of the number of looks to be used for coherence evaluation and a significant vertical resolution loss. In this paper, those factors will be taken into account to explicitly quantify the impact of bandwidth reduction on the retrieval of relevant forest parameters such as the forest height and the AGB. In order to do this, the forest height and the biomass have been estimated based on synthetic data emulating multibaseline BIOMASS acquisitions over the site of Paracou, French Guiana. Those data have been generated based on the P-band airborne data set collected by the Office National d'Etudes et de Recherches Aérospatiales (ONERA) in 2009 as a part of the ESA campaign TropiSAR [15]. Two different processing approaches have been considered. One approach consisted of degrading the resolution of the airborne data through the linear filtering of the raw data, followed by standard SAR processing. The other approach consisted of recovering the 3-D distribution of the scatterers at a high resolution, which was then reprojected onto the BIOMASS geometry.

This paper is organized as follows. Section II illustrates the basic principles of TomoSAR and the implications for BIOMASS. The generation of 6-MHz spaceborne data from airborne data is discussed in Section III. Results are presented and discussed in Section IV. Finally, conclusions are drawn in Section V.

II. BIOMASS Tomography

The rationale of TomoSAR is to employ multiple flight tracks, which are usually parallel to each other and characterized by small differences about the incidence angle. The ensemble of all flight lines allows us to form a synthetic aperture not only along each track but also in elevation. It follows that the signal can be integrated over a 2-D synthetic aperture, resulting in 3-D resolution capabilities [3], [6], [16]. The size of the resulting 3-D resolution cell is determined by the pulse bandwidth (PB) in the slant range direction and by the length of the synthetic aperture in the azimuth (along the track) and the elevation direction. With reference to Fig. 1, one can write

$$\begin{aligned} \triangle r &= \frac{c}{2B} \\ \triangle \xi &= \frac{R\lambda}{2A} \end{aligned} \tag{1}$$

where r is the slant range, ξ is the cross range, which is defined by the direction orthogonal to the radar LOS and the platform track, c is the speed of light, B is the transmitted bandwidth, λ is the radar wavelength, A is the baseline aperture (BA), and R is the sensor to target distance. The vertical resolution can be then obtained by considering the projection of the TomoSAR resolution cell onto the vertical direction. In the case where $\triangle\xi \gg \triangle r$, the vertical resolution is mainly limited by the BA as follows:

$$\triangle z = \triangle z^{(\mathrm{BA})} = \frac{R\lambda}{2A}\sin\theta \tag{2}$$

where θ is the incidence angle. In the opposite case ($\triangle r \gg \triangle\xi$), the vertical resolution is limited by the PB, leading to

$$\triangle z = \triangle z^{(\mathrm{PB})} = \frac{c}{2B}\cos\theta. \tag{3}$$

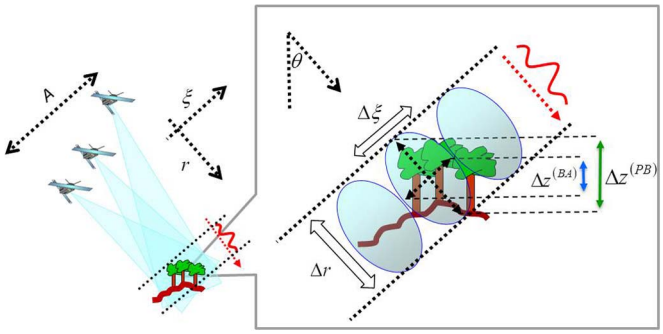

Fig. 1. Pictorial representation of the slant range and elevation extents of the resolution cell of a tomographic SAR system. Flight orbits are orthogonal to the picture.

TABLE I
BIOMASS Parameters for Simulation

Item	Characteristics
Satellite altitude	650 km
Incidence angle	25°
Carrier frequency	435 MHz
Bandwidth	6 MHz
Critical baseline	4610 m
Range resolution	25 m
Azimuth resolution	12.5 m
Number of tracks	6
Baseline aperture	Critical baseline

Relevant BIOMASS parameters are collected in Table I.

The system is assumed to operate at an incidence angle $\theta = 25°$, whereas its bandwidth is limited to 6 MHz by the ITU regulations [1]. Plugging these parameters into (3), one readily gets that the vertical resolution is limited by the PB to about 20 m. It follows that operating with arbitrary large BAs would not bring any advantage concerning the imaging of forested areas, with the vertical resolution being limited by (3). Interestingly, by equating the limits in (2) and (3), one gets that

$$A = \frac{B}{f_0}\mathrm{R}\tan\theta = b_{\mathrm{crit}} \tag{4}$$

where f_0 is the carrier frequency, and b_{crit} is the critical baseline. Accordingly, there are no reasons why the total BA should significantly exceed the critical baseline. For BIOMASS, this translates into an overall BA of about 4600 m.

The number of passes (or baselines) required to obtain the correct imaging of the illuminated forest is straightforwardly determined by considering that baseline sampling determines

ambiguous imaging in elevation exactly the same way as along-track sampling determines azimuth ambiguities in conventional 2-D SAR focusing. Assuming uniform baseline sampling, the height of ambiguity is obtained as [17]

$$z_{\text{amb}} = \frac{R\lambda}{2b_{\min}} \sin\theta \tag{5}$$

where $b_{\min}$ is the minimum baseline of the data set (i.e., baseline sampling). The height of ambiguity has to be larger than the expected forest height to avoid the superposition of the replicas. A safe choice is typically to set the height of ambiguity equal to at least twice the forest height [7]. Assuming a vegetation layer with a top height of 50 m, the resulting number of passages for tomographic imaging can be assessed in about six (the height of ambiguity $z_{\text{amb}} = 110$ m) per site, letting the overall BA equal the critical baseline. More passages can be exploited to enhance system robustness versus ionospheric disturbances [12] and severe weather conditions [13], [14].

III. Emulating BIOMASS Data From Airborne Data

Equations (2) and (3) show that the vertical resolution of a tomographic SAR system strongly depends on the incidence angle. Such dependence poses a fundamental problem in the case where a multibaseline spaceborne data set has to be emulated based on a multibaseline airborne data set. In fact, due to the huge difference about the flight height, the incidence angle of an airborne SAR can easily exhibit a variation on the order of 30° over a swath of few kilometers, whereas the incidence angle variation of a spaceborne SAR is limited to a few degrees. Accordingly, deriving a 6-MHz data set from an airborne data set by degrading the PB would produce a correct BIOMASS data set concerning the slant-range resolution, but it would not change the incidence angle variation along the swath. Another approach, which is the approach followed in this paper, consists of processing the available airborne data set through TomoSAR techniques in order to reconstruct the 3-D distribution of illuminated scatterers, which is afterward projected onto the spaceborne geometry accounting for system parameters (such as wavelength, bandwidth, etc.).

In the formula, let $s(x, y, z)$ represent the 3-D distribution of the scatterers (i.e., the output of TomoSAR processing), and let $d(r, x, b_n)$ represent a generic single-look complex (SLC) image of the simulated spaceborne data stack, where (r, x) indicates the range and azimuth coordinates, and b_n is the normal baseline. From the work in [17], neglecting system noise and atmospheric propagation, the relation between $d(r, x, b_n)$ and $s(x, y, z)$ is given by

$$d(r, x, b_n) = \int s(x', y', z') f(r - R_n, x - x') \times \exp\left(j\frac{4\pi}{\lambda} R_n\right) dx'dy'dz' \tag{6}$$

where $R_n = R_n(b_n, x', y', z')$ is the (zero-Doppler) distance between the target at (x', y', z') and the nth orbit, and $f(r, x)$ is the pulse response function of the spaceborne system. This equation provides a straightforward and reliable fashion to simulate the spaceborne data based on system geometry

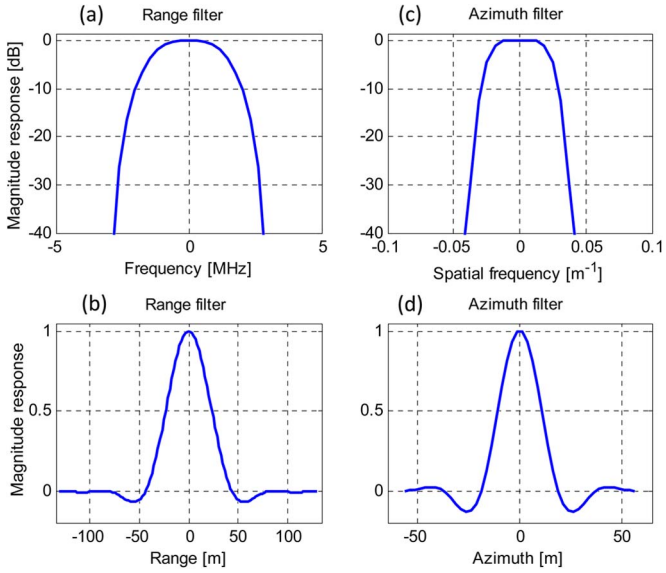

Fig. 2. Impulse response function for the BIOMASS SAR simulation. (a) and (b) Range filter in the frequency and the spatial frequency, respectively. (c) and (d) Azimuth filter in the frequency and the spatial frequency, respectively.

(embedded in $R_n(b_n, x', y', z')$) and sensor parameters, which are represented by $f(r, x)$. It is, however, important to note that the impact of the incidence angle of the airborne geometry is still present in the radiometric and polarimetric properties of the scatterers, which vary as a function of the incidence angle corresponding to the location of the scatterers in the original data set. In principle, this variation could be compensated for by resorting to the electromagnetic models of forest scattering [18], [19]. However, this point was not considered in this paper.

A. Impulse Response Function

The impulse response function is simulated through a separable model with respect to the azimuth and range axes, i.e.,

$$f(r, x) = f_r(r) \cdot f_a(x). \tag{7}$$

Range impulse response function f_r and azimuth f_a, both belonging to the raised-cosine function family [20], are shown in Fig. 2. The range pulse envelope has been modeled to ensure an attenuation of 40 dB at ± 3 MHz. This operation was done in order to mitigate as much sidelobes as possible, exceeding the portion of the frequency spectrum allowed for BIOMASS, although at the price of resolution loss.

IV. Results

This section is devoted to report the results obtained by processing a synthetic data set emulating multibaseline BIOMASS acquisitions over a tropical forest in Paracou, French Guiana.

A. Paracou Test Site

The Paracou experimental site is located in a lowland tropical rainforest near Sinnamary, French Guiana (5°18′N, 52°55′W) [21]. The elevation is between 5 and 50 m, and the mean annual temperature is 26 °C, with an annual range of 1 °C–1.5 °C. Rainfall averages 2980 mm/year (30-year period), with a three-month dry season (<100 mm/month) from mid-August

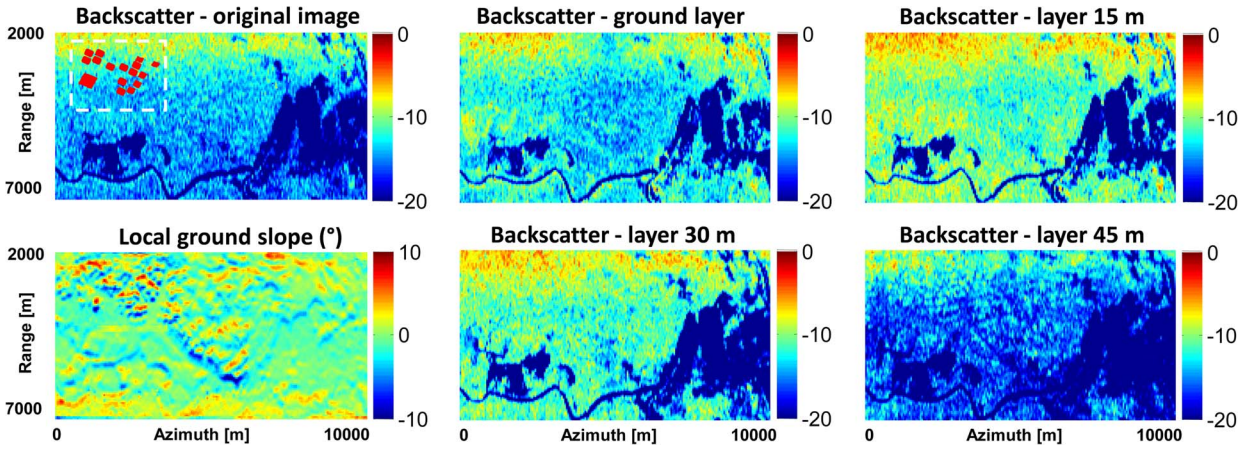

Fig. 3. Tomographic results from the 6-MHz airborne geometry: HV backscatter for four tomographic layers associated with four different heights above the ground, i.e., 0 (ground layer), 15, 30, and 45 m. The top-left panel presents the original HV image with red rectangles relative to areas where *in situ* AGB measurements are available and white dash rectangles relative to the area where LiDAR forest height data are available. The LiDAR coverage is about 2.5 and 3 km in the range and azimuth directions, respectively. The bottom-left panel is the local ground slope calculated using the procedure outlined in [7].

to mid-November [22]. The landscape is characterized by a patchwork of hills (100–300-m wide and 20–35-m high) separated by narrow streams. Slopes vary up to about 25°. The forest in Paracou is classified as a lowland moist forest with 140–200 species/ha, which are specified in the forest census of all trees with a diameter at breast height (DBH) >10 cm. The forest height ranges from 20 to 40 m.

To analyze the relationship between the tomographic data and the forest biomass, we use *in situ* forest measurements on 16 permanent plots established starting 1984 in the Paracou primary forest. These are 15 plots of 250 m × 250 m (6.25 ha) each and 1 plot of 500 m × 500 m (25 ha) in which all stems of the DBH ≥10 cm has been mapped and regularly surveyed since 1986. For the Paracou primary forests, the number of trees with DBH > 10 cm ranges between 400 to 700 stems/ha.

From 1986 to 1988, 9 of these 15 6.25-ha plots underwent three different logging treatments ranging from mild to severe for a study of the forest responses to logging intensities. In Treatment 1, selected timbers were extracted, with an average of ten trees with a DBH of 50 or 60 cm removed per hectare. Treatment 2 was logged as in Treatment 1, followed by timber stand improvement by the poison girdling of selected noncommercial species, with about 30 trees with a DBH of 40 cm removed per hectare. Treatment 3 was logged as in Treatment 2 for an expanded list of commercial species, with about 45 trees with a DBH of 40 cm removed per hectare. In 2009, the degraded plots had the AGB at a 1-ha resolution ranging from 250 to 392 t/ha, depending on the initial logging intensity [23].

LiDAR forest height data are available at Paracou. This was generated from the cloud data at 1-m resolution using the Fusion software [24]. The LiDAR coverage is about 2.5 and 3 km in range and azimuth directions, respectively. This covers all 16 *in situ* permanent plots for the comparison study.

B. Emulated BIOMASS Data Set

The emulated BIOMASS data set was derived from the P-band airborne data set collected by ONERA in 2009 as a part of the ESA campaign TropiSAR [15]. The resolution is about 1 m in the slant range (125-MHz bandwidth) and 1.245 m in the azimuth. This data set is characterized by an almost constant vertical resolution of about 20 m, whereas the forest height ranges from 20 to 40 m. Owing to these features, the 3-D distribution of the scene complex reflectivity can be mapped in up to three independent layers by a coherent focusing without making physical assumptions nor employing superresolution techniques. Tomographic analyses of this data set were presented in [7], [25], and [26], which the reader is referred to for details.

The emulated BIOMASS data set discussed in this paper was obtained according to the procedure in Section III, where the high-resolution 3-D distribution of the scatterers [term $s(x, y, z)$ in (6)] was obtained, as described in [7]. The emulated data set consists of six BIOMASS passes. The overall BA was chosen to equal the critical baseline. Baseline sampling is done to ensure a height of ambiguity equal to 110 m [see Table I and (5)].

For the sake of completeness, another 6-MHz data set was generated by reducing the range and azimuth resolutions of the airborne data set through linear filtering. This is also provided by ONERA. These two 6-MHz data sets will be hereinafter referred to as 6-MHz *spaceborne* geometry and 6-MHz *airborne* geometry, respectively. For both data sets, the subsequent tomographic processing consisted of converting the emulated multibaseline data set into a multilayer data set, where each layer represents the complex scene reflectivity associated with a certain height above the ground.

Fig. 3 shows the HV backscatter for the layer at the four levels in the 6-MHz airborne geometry, displaying different information contents. The results are observed to be consistent with the results obtained in the full-bandwidth (125 MHz) case (see [7, Fig. 4]), where the zoom version of the white dash rectangle area was shown. At such an area, in Fig. 4, the joint distribution of the terrain ground slope and the HV tomographic backscatter in the 6-MHz airborne geometry is shown. The white line denotes the linear fit. For the ground slope varying from -10° to 10°, the regression has a slope of about 3.5, 2, 2, and 5 dB at the ground layer (0 m), the 15-m layer, the

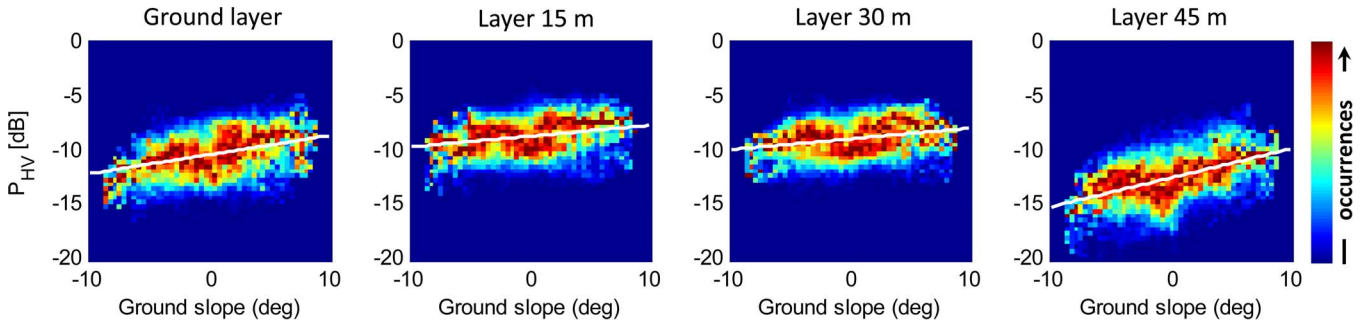

Fig. 4. Joint distribution of the terrain ground slope and the HV tomographic backscatter in the 6-MHz airborne geometry. All panels have been normalized such that the maximum (red) along each column is unitary. The white line denotes the linear fit.

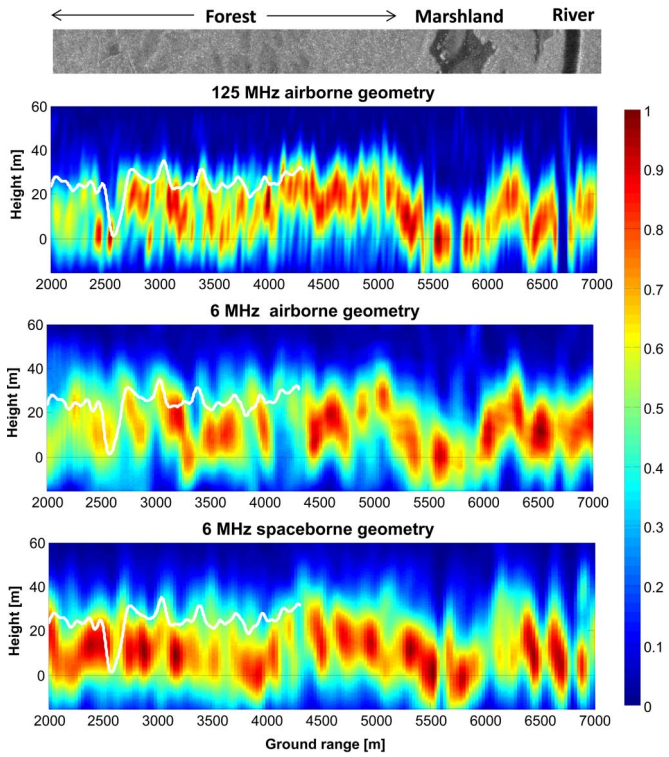

Fig. 5. Tomographic reconstruction along the same azimuth cut in HV polarizations at 125 and 6 MHz in both the spaceborne geometry and the airborne geometry. The white line denotes the LiDAR height measurements. All panels have been normalized in such a way that the sum along the height is unitary.

30-m layer, and the 45-m layer, respectively. Hence, the ground layer and the top layer (45 m) show strong topographic effects, whereas the middle layers (at 15 and 30 m) are less affected by the topography. Further processing steps, such as topographic compensation and geocoding to investigate the relationship with the *in situ* measurement, are carried out according to the procedure proposed in [7].

C. Tomographic Profiles

Tomographic profile results are reported here based on the retrieved 3-D backscatter distributions from the multilayer SLC for a single azimuth transect. In Fig. 5, the top panel shows a strip of the P-band SAR image over the forest, the marshland, and the river. In other panels, the white line denotes the LiDAR height measurements for comparison with the tomography profile. The color panels show a tomographic transect over this region, i.e., the vertical distribution of the backscatter intensity displayed in HV polarization at 125 and 6 MHz with both the spaceborne geometry and the airborne geometry. In order to facilitate visualization with LiDAR height measurements, the tomographic profiles have been normalized in such a way that the sum along the height is unitary. Over the forests, at 6 MHz with both the spaceborne geometry and the airborne geometry, the backscatter from the canopy is dominant and visible.

The reduction of the bandwidth to 6 from 125 MHz in both approaches is evident in the loss in horizontal resolution; however, the loss in vertical resolution, although present and visible, is not really critical. The vertical resolution is still significantly lower than the forest height in tropical forests. The most relevant difference between the 6-MHz airborne and spaceborne data sets is relatively observed to the vertical profiles, in that the airborne geometry data are clearly affected by a varying vertical resolution in the range direction.

D. Relation to Forest Biomass

The analysis in this section is carried out by evaluating the correlation between the *in situ* AGB and backscatter at different heights. As it is shown in [7] and [27], in all polarizations, the HV upper layer exhibits the best correlation with the AGB. We then focus on presenting HV results in the remainder. For comparison, we report the results obtained at the 125-MHz case in Fig. 6. This displays the backscatter in HV for the 16 plots where *in situ* AGB measurements are available, with 9 layers varying from 0 to 40 m at 5-m intervals. At the size of the 6.25-ha (250 m $\times$ 250 m) plots, we expect the number of looks in both 6-MHz data sets to be greater than 85. In Fig. 7, the 6-MHz results in both the spaceborne geometry and the airborne geometry are shown.

The quality of the correlation is assessed using Pearson linear correlation r_P [28], which measures the degree of association between the *in situ* AGB and backscatter. It is actually interesting to note that, unlike for the top layers, the backscatter from the bottom layers is negatively correlated with the AGB so that the Pearson's correlation coefficient has been preferred to the coefficient of determination (always positive) in order to catch this difference of behavior. For the layers under 20 m, the Pearson linear correlation r_P between the backscatter and the AGB is very weak (and negative in the 6-MHz airborne geometry case). On the contrary, for layers from 20 to 40 m,

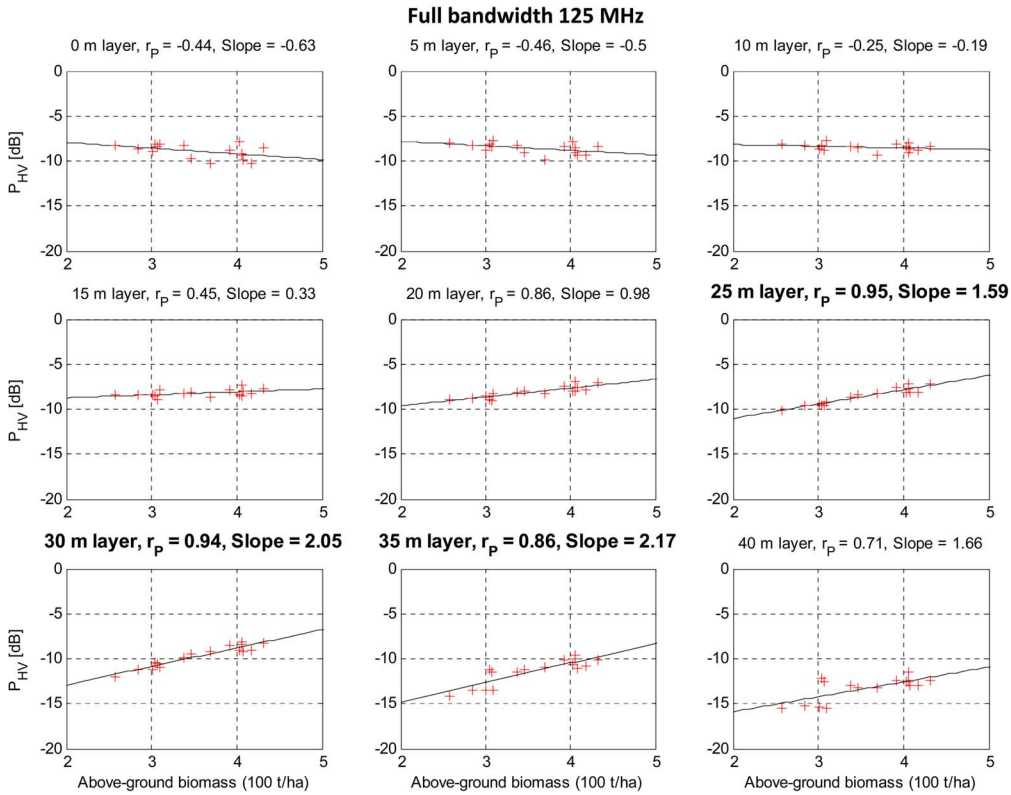

Fig. 6. Sensitivity of the backscatter power at different layers to the AGB in the HV channel at a full bandwidth of 125 MHz. r_P is the Pearson correlation coefficient. Slope is referred to the angular coefficient of the linear regression. The bold title at the 25-, 30-, and 35-m layers indicates not only that the correlation between the backscatter and the AGB becomes highly significant but also that the backscatter dynamic range is larger.

the correlation between the backscatter and the AGB becomes highly significant.

In both approaches, the 30-m layer has a similar behavior. This layer exhibits a correlation at the highest value with *in situ* data and no bias phenomena over the AGB values ranging from 250 to 450 t/ha. At the 35-m layer, the backscatter dynamic range is larger; however, the correlation is reduced, and the dispersion is increased. For the top layer (40 m), the correlation decreases, and the dispersion increases as well.

Accordingly, results at 6 MHz in both the spaceborne geometry and the airborne geometry appear to be well consistent with those observed in the 125-MHz case, indicating that the 30-m layer appears to be the most informative about the AGB. The physical reasons behind this behavior were discussed in [7], which the reader is referred to for details. For the sake of completeness, here, we summarize the main conclusions.

- For layers below 20 m, the correlation between the backscattered power and the AGB is very weak (and with a negative trend). This can be explained by the following: 1) the trend is negative because of extinction, in that the higher the trees, the weaker the signal penetrating down to the ground; and 2) the scatter plots are dispersed since the dominant scattering mechanisms may drastically change when the ground surface is tilted relative to the horizontal.
- For layers between 20 and 40 m, the correlation between the backscatter and the AGB becomes highly significant, implying that: 1) the perturbing effect of the ground contribution is minimized (i.e., TomoSAR focusing allows a very good rejection of ground contributions); and 2) there is a strong correlation between the biomass contained in this layer and the total AGB.

As in [7], we define a simple AGB estimator assuming the following log law:

$$\mathrm{AGB} = a \cdot \log_{10}(P_{30}) + b \tag{8}$$

where AGB is the estimated forest AGB, P_{30} is the HV backscatter at 30 m, and a, b are two parameters to be fixed using training data.

The results are shown in Fig. 8. In the 125-MHz case, this method yielded an RMS error (RMSE) of 5%. In the 6-MHz case, the RMSE turned out to be 10% in both the spaceborne geometry and the airborne geometry due to the significant spatial resolution loss.

E. Forest Height Estimation

The retrieval of forest height has been assessed through a direct investigation of a tomographic profile, i.e., the shape of the 3-D backscatter distribution from the multilayer SLC at each location.

The criterion adopted in assessing the forest height follows after the basic assumption that the shape of the backscatter distribution can be roughly divided into three zones (see Fig. 9). One zone is found in the correspondence of the phase center location, where most of the backscatter is concentrated. Then, the backscatter undergoes a loss due to both the point spread function of the tomographic processors and the (eventual)

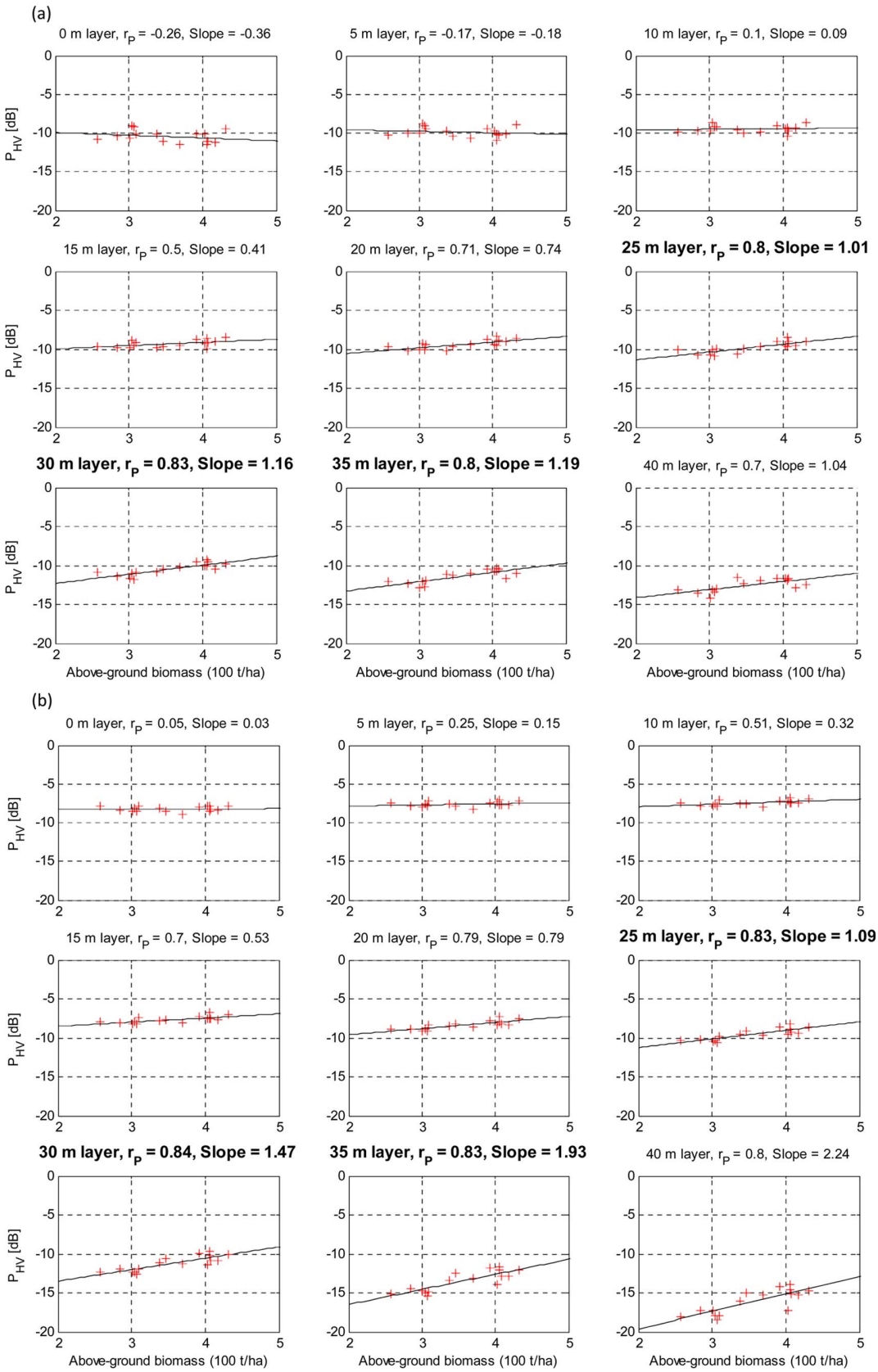

Fig. 7. Sensitivity of the backscatter power at different layers to the AGB in the HV channel in both the spaceborne geometry and the airborne geometry. r_P is the Pearson correlation coefficient. Slope is referred to the angular coefficient of the linear regression. (a) 6-MHz airborne geometry. (b) 6-MHz spaceborne geometry. The bold title at the 25-, 30-, and 35-m layers indicates not only that the correlation between the backscatter and the AGB becomes highly significant but also that the backscatter dynamic range is larger.

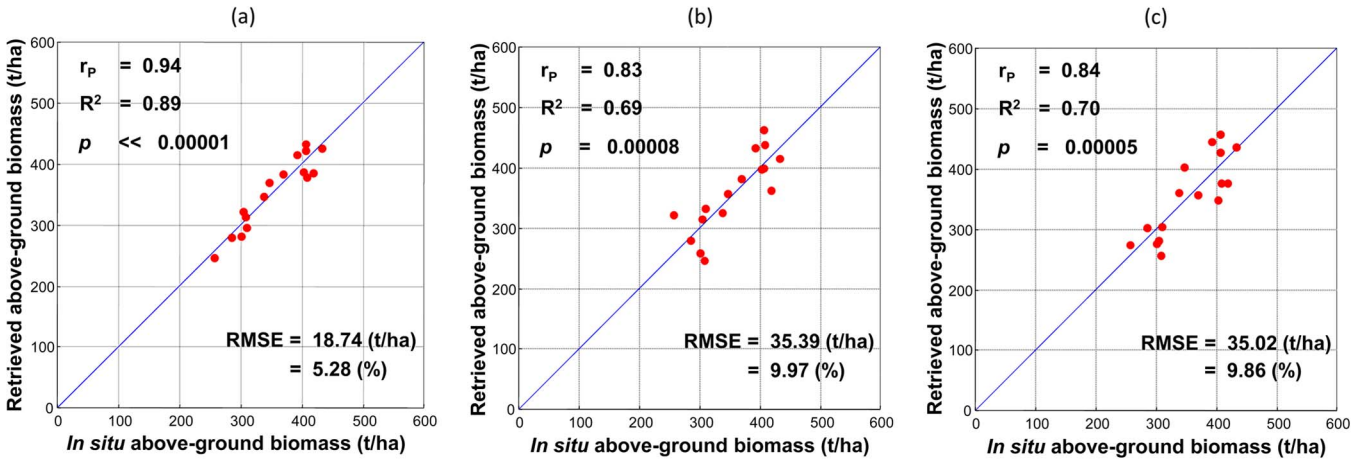

Fig. 8. Comparison between the *in situ* biomass and the biomass derived from the inversion of the P-band HV 30-m layer in the full-bandwidth 125-MHz case and in both the spaceborne geometry and the airborne geometry. (a) Full bandwidth of 125 MHz. (b) 6-MHz airborne geometry. (c) 6-MHz spaceborne geometry. The RMSE, Pearson linear correlation r_P, the coefficient of determination R^2, and the p value are reported.

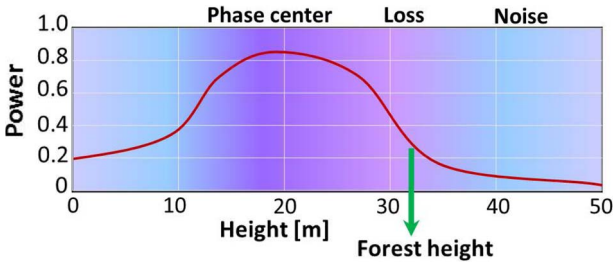

Fig. 9. Schematic view of the vertical backscatter distribution for the retrieval of forest height. This can be roughly divided into the phase center, loss, and noise zones, in which the loss zone can be used to estimate the forest height.

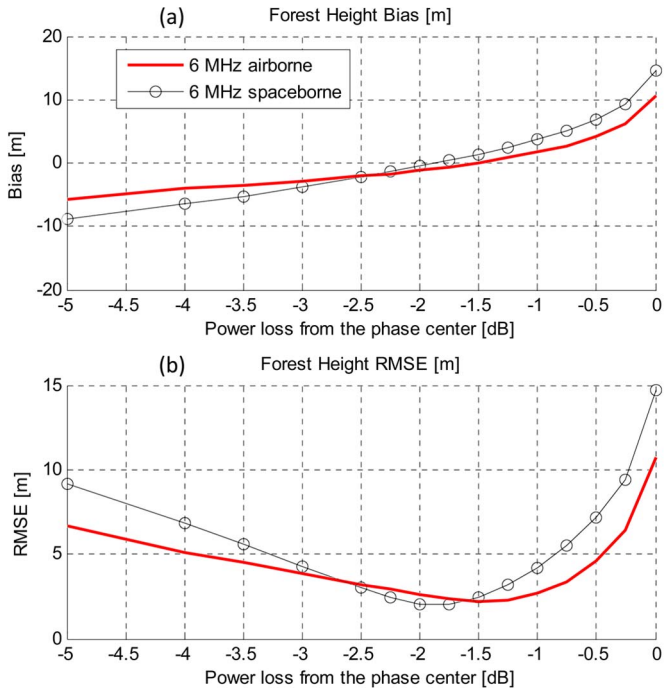

Fig. 10. Error about the forest height versus the power loss with respect to the phase center elevation. (a) Bias. (b) RMSE.

tapering of the forest density. Further away along the vertical direction, the backscatter is mostly contributed by noise, resulting in this zone not to be likely associated with physically relevant components. Accordingly, the forest height has been retrieved by evaluating the power loss from the phase center location in the upper envelope of the profile [6].

In Fig. 10, we have evaluated the forest height location corresponding to a power loss with respect to the phase center ranging from 0 to -5 dB. The results report the bias and the RMSE with respect to the LiDAR measurements. For both the spaceborne geometry and the airborne geometry, at a power loss of about -1.75 dB, the RMSE has turned out to be about 2.5 m.

LiDAR forest height H_{LiDAR} is shown in Fig. 11(a) to facilitate the interpretation of the results from the tomography. In Fig. 11(b) and (c), an agreement of tomographic forest height $H_{\mathrm{tomography}}$ with the LiDAR measurements is shown for the 6-MHz airborne geometry and the 6-MHz spaceborne geometry, respectively. Both the LiDAR and tomographic forest heights are filtered using an averaging window of 100 m $\times$ 100 m. The relative error has been evaluated as $|H_{\mathrm{tomography}} - H_{\mathrm{LiDAR}}|/H_{\mathrm{LiDAR}}$. The average relative error is 13% and 10% for the 6-MHz airborne geometry and the 6-MHz spaceborne geometry, respectively.

The joint distribution of the forest height is shown in Fig. 12. The joint distribution has been normalized such that the maximum is unitary along each column. The estimation appears to be reliable for vegetation layers ranging from 20 to 30–35 m, which is consistent with the forest height of tropical forest areas. For this range height, the standard deviation of the forest height estimated from TomoSAR with respect to LiDAR has been assessed as less than 4 m. It is worth noting that the estimation loses sensitivity for a forest height below 15 m as a consequence of the fact that the vertical resolution for BIOMASS is bounded by the PB to about 20 m. Better results could be obtained by employing a more sophisticated tomographic processor and/or model-based methods (see [6]).

V. Discussions and Conclusion

This paper has focused on assessing the performance of the P-band multibaseline TomoSAR about the retrieval of forest biomass and height in tropical forests, accounting for the

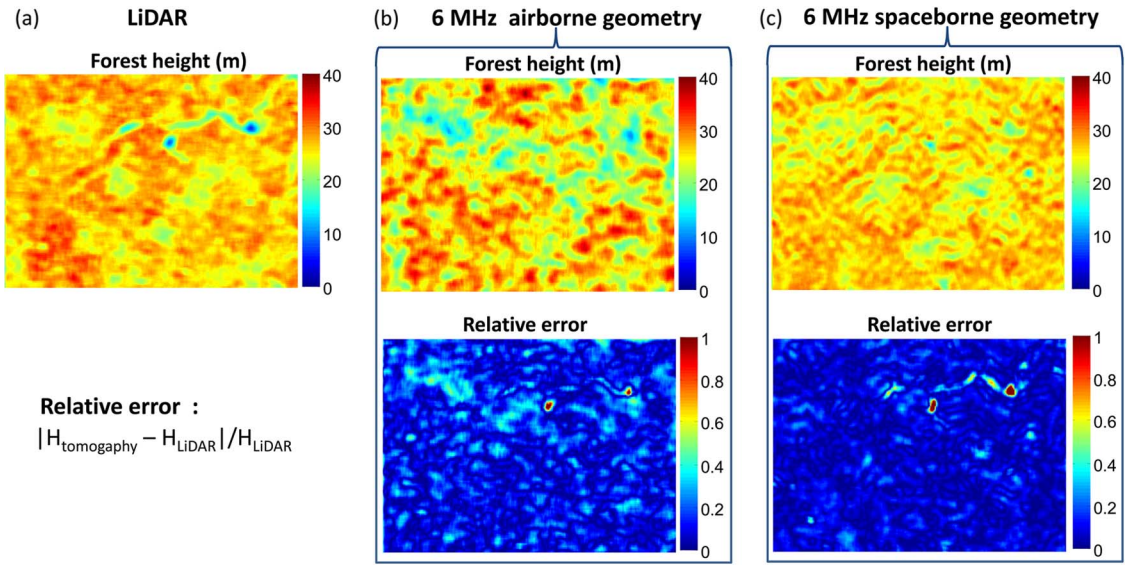

Fig. 11. Comparison between the LiDAR and tomography retrieval of the forest height in both the spaceborne geometry and the airborne geometry. (a) LiDAR forest height available is shown, as in Fig. 3, which is about 2.5 and 3 km in the vertical and horizontal directions, respectively. (b) 6-MHz airborne geometry (top panel: forest height; bottom panel: relative error). (c) 6-MHz spaceborne geometry (top panel: forest height; bottom panel: relative error).

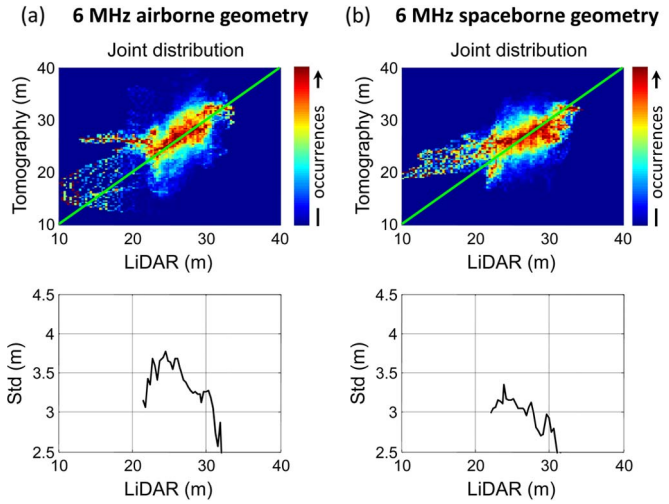

Fig. 12. Joint distribution between the LiDAR and tomography retrieval of the forest height in both the spaceborne geometry and the airborne geometry. (a) 6-MHz airborne geometry [top panel: distribution; bottom panel: standard deviation (std)]. (b) 6-MHz spaceborne geometry [top panel: distribution; bottom panel: standard deviation (std)]. The joint distribution has been normalized such that the maximum (red) is unitary along each column.

6-MHz bandwidth limitation imposed by the ITU regulations to the BIOMASS mission.

The data considered in this paper have been derived from the airborne data set TropiSAR. Two different types of 6-MHz data were considered. The 6-MHz airborne geometry data were derived by degrading the resolution of the airborne data through linear filtering. The 6-MHz spaceborne geometry data were derived by first recovering the 3-D distribution of the scatterers at a high resolution, which was then backprojected onto the BIOMASS geometry, accounting for the available radio-frequency bandwidth. This procedure allows us to obtain a data stack that is consistent with BIOMASS concerning not only the spatial resolution but also the system incidence angle. The same TomoSAR processor was used to process both the airborne and spaceborne geometry data sets, resulting in two data cubes providing a 3-D reconstruction of the Paracou forest site at 6 MHz.

The loss in vertical resolution from both approaches due to reducing the bandwidth is evident, but it is not critical. The vertical resolution is still significantly smaller than the forest height in tropical forests. The most relevant difference between the airborne and spaceborne data sets was observed relative to the vertical profiles yielded by the TomoSAR processor, in that the airborne geometry data were clearly affected by a varying vertical resolution with respect to the range.

No relevant difference was observed between the 6-MHz airborne and spaceborne cases concerning the sensitivity to the AGB, as obtained through *in situ* measurements over 16 plots. The 30-m layer was found to exhibit a correlation value with respect to the AGB higher than 0.8 and no bias phenomena over the AGB values ranging from 250 to 450 t/ha. This result is consistent with the result obtained by processing the full-bandwidth (125 MHz) TropiSAR data [7].

An estimator was defined to retrieve the AGB based on the HV backscatter at 30 m above the ground. The accuracy of the AGB retrieval based on the BIOMASS tomographic data turned out to be about 10% at a 6.25-ha resolution. The forest height was estimated by tracing the upper envelope of the TomoSAR vertical profiles, as averaged over a 100 m $\times$ 100 m window. Height estimation turned out to be reliable for vegetation layers ranging from 20 to 30–35 m, which is consistent with the relatively high forest height in tropical forest areas. For this range of forest height, the standard deviation has been assessed as less than 4 m.

The results of this paper have proven that the 6-MHz bandwidth limitation is not a showstopper concerning the TomoSAR analyses of tropical forests. This can be qualitatively understood by considering that the 6-MHz bandwidth configuration at a 25° incidence angle results in a ground range resolution on the order of 60 m (assuming a flat terrain) and a vertical

resolution on the order of 20 m. Accordingly, TomoSAR processing can be successfully employed to decompose the backscatter from a tropical forest into two–three layers and, hence, provide valuable information about the forest vertical structure.

We note that the same conclusion cannot be straightforwardly extended to the case of boreal forests, whose average height is about 20 m, despite the good height retrieval results obtained at 6 MHz in the frame of the BioSAR 2008 campaign [6].

Finally, the BIOMASS mission is ongoing with the phase-B1/B2, in which the tomographic mode is designed to be operated for one year, resulting in one global coverage. Therefore, to provide complete performance assessments for the tomography in BIOMASS, much work remains to be done. Future analysis needs to account for ionospheric disturbances, temporal decorrelation, environment effect such as rain, and the limitation of the biomass retrieval method in low biomass forests.

ACKNOWLEDGMENT

The authors would like to thank the entire TropiSAR 2009 Team and Dr. L. Blanc for providing the *in situ* data.

REFERENCES

[1] "Report for mission selection: BIOMASS," Paris, France, ESA SP-1324/1, May 2012.

[2] T. Le Toan *et al.*, "The BIOMASS Mission: Mapping global forest biomass to better understand the terrestrial carbon cycle," *Remote Sens. Environ.*, vol. 115, no. 11, pp. 2850–2860, Nov. 2011.

[3] A. Reigber and A. Moreira, "First demonstration of airborne SAR tomography using multibaseline L-band data," *IEEE Trans. Geosci. Remote Sens.*, vol. 38, no. 5, pp. 2142–2152, Sep. 2000.

[4] R. N. Treuhaft and P. R. Siqueira, "Vertical structure of vegetated land surfaces from interferometric and polarimetric radar," *Radio Sci.*, vol. 35, no. 1, pp. 141–177, Feb. 2000.

[5] G. Fornaro and F. Serafino, "Imaging of single and double scatterers in urban areas via SAR tomography," *IEEE Trans. Geosci. Remote Sens.*, vol. 44, no. 12, pp. 3497–3505, Dec. 2006.

[6] S. Tebaldini and F. Rocca, "Multibaseline polarimetric SAR tomography of a boreal forest at P- and L-Bands," *IEEE Trans. Geosci. Remote Sens.*, vol. 50, no. 1, pp. 232–246, Jan. 2012.

[7] D. Ho Tong Minh *et al.*, "Relating P-band synthetic aperture radar tomography to tropical forest biomass," *IEEE Trans. Geosci. Remote Sens.*, vol. 52, no. 2, pp. 967–979, Feb. 2014.

[8] *Article 5 (Frequency Allocations) of the Radio Regulations*, ITU-2004, International Telecommunication Union, 2014.

[9] S. Quegan and J. Lamont, "Ionospheric and tropospheric effects on synthetic aperture radar performance," *Int. J. Remote Sens.*, vol. 7, no. 4, pp. 525–539, Apr. 1986.

[10] S. Quegan, J. Green, R. Zandona-Schneider, R. Scheiber, and K. Papathanassiou, "Quantifying and correcting ionospheric effects on P-band SAR images," in *Proc. IEEE IGARSS*, Jul. 2008, vol. 2, pp. II-541–II-544.

[11] F. Rocca, "Modeling interferogram stacks," *IEEE Trans. Geosci. Remote Sens.*, vol. 45, no. 10, pp. 3289–3299, Oct. 2007.

[12] S. Tebaldini and L. Iannini, "Assessing the performance of tomographic measurements from a P-band spaceborne SAR," presented at the 9th EUSAR, Apr. 2012.

[13] D. Ho Tong Minh *et al.*, "Ground-based array for tomographic imaging of the tropical forest in P-band," *IEEE Trans. Geosci. Remote Sens.*, vol. 51, no. 8, pp. 4460–4472, Aug. 2013.

[14] D. Ho Tong Minh *et al.*, "Vertical structure of P-Band temporal decorrelation at the Paracou forest: Results from TropiScat," *IEEE Geosci. Remote Sens. Lett.*, vol. 11, no. 8, pp. 1438–1442, Aug. 2014.

[15] P. C. Dubois-Fernandez *et al.*, "The TropiSAR airborne campaign in French Guiana: Objectives, description, and observed temporal behavior of the backscatter signal," *IEEE Trans. Geosci. Remote Sens.*, vol. 50, no. 8, pp. 3228–3241, Aug. 2012.

[16] O. Frey and E. Meier, "Analyzing tomographic SAR data of a forest with respect to frequency, polarization, and focusing technique," *IEEE Trans. Geosci. Remote Sens.*, vol. 49, no. 10, pp. 3648–3659, Oct. 2011.

[17] R. Bamler and P. Hartl, "Synthetic Aperture Radar Interferometry," *Inverse Probl.*, vol. 14, no. 4, pp. R1–R54, Aug. 1998.

[18] S. Durden, J. Van Zyl, and H. Zebker, "Modeling and observation of the radar polarization signature of forested areas," *IEEE Trans. Geosci. Remote Sens.*, vol. 27, no. 3, pp. 290–301, May 1989.

[19] M. Karam, A. Fung, R. Lang, and N. Chauhan, "A microwave scattering model for layered vegetation," *IEEE Trans. Geosci. Remote Sens.*, vol. 30, no. 4, pp. 767–784, Jul. 1992.

[20] P. S. R. Diniz, E. A. B. da Silva, and S. L. Netto, *Digital Signal Processing System Analysis and Design*. Cambridge, U.K.: Cambridge Univ. Press, 2010.

[21] Gourlet-Fleury, S. J.-M. Guehl, and O. Laroussinie, *Ecology and Management of a Neotropical Forest, Lessons Drawn From Paracou, a Long-Term Experimental Research Site in French Guiana*. Paris, France: Elsevier, 2004.

[22] D. Epron, A. Bosc, L. D. Bona, and V. Freycon, "Spatial variation of soil respiration across a topographic gradient in a tropical rain forest in French Guiana," *J. Tropical Ecol.*, vol. 22, no. 5, pp. 565–574, Sep. 2006.

[23] P. Dubois-Fernandez *et al.*, "Tropisar 2009 technical assistance for the development of airborne SAR and geophysical measurements during the TropiSAR 2009 experiment," Eur. Space Agency (ESA), Paris, France, ESA CONTRACT No. 22446/09/NL/CT, CNES CONTRACT No. 92929 03/08/09, Feb. 2011.

[24] R. McGaughey, "Fusion/ldv: Software for Lidar data analysis and visualization," US Dept. Agric., Forest Service, Pacific Northwest Res. Station, Seattle, WA, USA, 2012.

[25] M. Mariotti d'Alessandro and S. Tebaldini, "Phenomenology of P-Band scattering from a tropical forest through 3-D SAR tomography," *IEEE Geosci. Remote Sens. Lett.*, vol. 9, no. 3, pp. 442–446, May 2012.

[26] M. Mariotti d'Alessandro, S. Tebaldini, and F. Rocca, "Phenomenology of ground scattering in a tropical forest through polarimetric synthetic aperture radar tomography," *IEEE Trans. Geosci. Remote Sens.*, vol. 51, no. 8, pp. 4430–4437, Aug. 2013.

[27] D. Ho Tong Minh, F. Rocca, S. Tebaldini, M. Mariotti d'Alessandro, and T. Le Toan, "Linear and circular polarization P band SAR tomography for tropical forest biomass study," in *Proc. 9th EUSAR*, Apr. 2012, pp. 489–492.

[28] H. Klugh, *Statistics: The Essentials for Research*. Mahwah, NY, USA: Lawrence Erlbaum, 1986.